Supplementary Information: A machine learning model that outperforms conventional global subseasonal forecast models

Lei Chen[1,2†], Xiaohui Zhong[1†], Hao Li[1*†], Jie Wu[3†], Bo Lu[3,4*], Deliang Chen[5], Shang-Ping Xie[6], Libo Wu[7,8,9], Qingchen Chao[3], Chensen Lin[1], Zixin Hu[1] and Yuan Qi[2,1*]

[1]Artificial Intelligence Innovation and Incubation Institute, Fudan University, Shanghai, 200433, China.
[2]Shanghai Academy of Artificial Intelligence for Science, Shanghai, 200232, China.
[3]China Meteorological Administration Key Laboratory for Climate Prediction Studies, National Climate Center, Beijing, 100081, China.
[4]Xiong'an Institute of Meteorological Artificial Intelligence, Xiong'an, China.
[5]University of Gothenburg, Sweden.
[6]Scripps Institution of Oceanography, University of California San Diego, USA.
[7]School of Data Science, Fudan University, Shanghai, 200433, China.
[8]Institute for Big Data, Fudan University, Shanghai, 200433, China.
[9]MOE Laboratory for National Development and Intelligent Governance, Fudan University, Shanghai, 200433, China.

*Corresponding author(s). E-mail(s): lihao_lh@fudan.edu.cn; bolu@cma.gov.cn; qiyuan@fudan.edu.cn;
Contributing authors: cltpys@163.com; x7zhong@gmail.com; wujie@cma.gov.com; deliang@gvc.gu.se; sxie@ucsd.edu;

wulibo@fudan.edu.cn; chaoqc@cma.gov.cn;
linchensen@fudan.edu.cn; huzixin@fudan.edu.cn;
†These authors contributed equally to this work.

Contents of this file

Supplementary Notes

1 Effectiveness of flow-dependent perturbations

This section discusses the effect of incorporating the flow-dependent perturbations into the model's hidden features to enhance performance in subseasonal forecasts. We conducted experiments using FuXi-S2S models which exclusively employ Perlin noise in the initial conditions or combine Perlin noise in the initial conditions with fixed perturbations added into the hidden features, to generate 42-day forecasts. Subsequently we evaluate their performance in comparison with the original FuXi-S2S model.

Supplementary Figure 1 presents a comparison of the globally-averaged and latitude-weighted TCC for TP. This analysis encompasses all testing data from the period spanning from 2017 to 2021. The FuXi-S2S model, which incorporates flow-dependent perturbations into its hidden features, consistently exhibits considerably improved forecast performance in comparison to the FuXi-S2S model that incorporates fixed Gaussian noise into the hidden features, across all forecast lead times. Furthermore, the introduction of flow-dependent perturbations has extended the FuXi-S2S model's skillful MJO prediction from 22 days to 36 days.

2 Deterministic forecast metrics comparison

Supplementary Figure 3 presents a comparison of latitude-weighted TCC between FuXi-S2S and ECMWF S2S. It examines TP, T2M, Z500, and OLR across four geographical regions: in the extra-tropics (90°S - 30°S and 30°N - 90°N), in the tropics (30°S - 30°N), over land, and over the ocean. Within the extra-tropical regions, FuXi-S2S consistently exhibits superior performance compared to ECMWF S2S for all four variables. In tropical regions, FuXi-S2S outperforms ECMWF S2S for TP and OLR, while achieving comparable accuracy in T2M and Z500. Over land areas, FuXi-S2S demonstrates consistently higher TCC values for TP, Z500, and OLR.

Supplementary Figure 4 presents a comparison of the globally-averaged and latitude-weighted root mean square error (RMSE) of the ensemble mean between ECMWF S2S real-time forecasts and FuXi-S2S forecasts for total precipitation (TP), 2-meter temperature (T2M), geopotential at 500 hPa (Z500), and outgoing longwave radiation (OLR). The analysis is derived from the averaged RMSE computed using testing data from the year 2022. FuXi-S2S demonstrates superior forecast performance for all four variables across all forecast lead times compared to ECMWF S2S, consistently achieving lower RMSE values than ECMWF S2S.

Supplementary Figure 5 presents the energy spectra of T2M, Z500, TP, and OLR at seven forecast lead times: 1, 8, 15, 22, 29, 36, and 42 days). This figure demonstrates the effectiveness of the models by showcasing the energy levels across various scales and lead times. The spectra are calculated and presented for both the ensemble mean and a randomly selected ensemble member from the ECMWF S2S reforecasts and FuXi-S2S forecasts. The ERA5 spectra remain consistent across increasing forecast lead times, serving as a baseline to evaluate whether the forecasts become increasingly smoother as the forecast lead times increases. Remarkably, at longer wavelengths, a randomly selected member from either the FuXi-S2S or ECMWF S2S models shows closer alignment with the ERA5 benchmark, suggesting that both models proficiently predict the dominant, larger-scale motions. However, at shorter wavelengths, the FuXi-S2S model initially matches the ERA5 spectra but shows a gradual reduction in energy as forecast lead times increase, indicating increasingly smoother forecasts at smaller scales. In contrast, an ECMWF S2S ensemble member maintains consistent agreement at these smaller scales. Regarding the ensemble mean, both the ECMWF S2S reforecasts and FuXi-S2S forecasts generally exhibit lower energy spectra levels at most forecast lead times compared to both ERA5 data and individual ensemble members. As the lead time increases, the ensemble mean of both models demonstrate a decline in performance at smaller scales, a degradation more significant than that observed in individual ensemble members of the FuXi-S2S model. The notably lower energy levels in the FuXi-S2S model, particularly at longer forecast lead times compared to the ECMWF S2S and ERA5 data, underscore a critical area for model improvement to enhance forecast accuracy and smoothness.

3 Ensemble forecast metrics comparison

Supplementary Figure 8 compares the globally-averaged and latitude-weighted RMSE, ensemble spread, and spread skill ratio (SSR) between ECMWF S2S reforecasts and FuXi-S2S forecasts for TP, T2M, Z500, and sea surface temperature (SST). These metrics are derived from daily mean forecasts, calculated using all available testing data from 2017 to 2021 as a function of forecast lead times. For TP, FuXi-S2S consistently outperforms ECMWF S2S in terms of RMSE. For SST, FuXi-S2S initially shows slightly superior performance compared to ECMWF S2S for the forecast lead times of 15 to 20 days, but its performance declines relative to ECMWF S2S thereafter. In terms of ensemble spread, FuXi-S2S generally shows smaller spread than ECMWF S2S for both TP and SST. However, their SSR values are consistently lower than those of ECMWF S2S across all forecast lead times, suggesting that the ensemble spread of ECMWF S2S more accurately predicts forecast skill for these variables. For T2M, FuXi-S2S demonstrates SSR values closer to 1 compared to ECMWF S2S during the forecast lead times from 20 to 42 days, indicating a higher reliability of ensemble spread. Overall, both ECMWF S2S and FuXi-S2S have SSR values below 1 for all 4 evaluated variables across all forecast lead times, suggesting underdispersion. This result suggests that there is still room for improvement in the FuXi-S2S to achieve SSR closer to 1.

4 MJO predictions

The Madden-Julian Oscillation (MJO) stimulates several important teleconnection patterns, such as the Pacific-North American (PNA) pattern, which profoundly impacts extratropical anomalies. Therefore, accurately simulating MJO-related teleconnections is crucial for effective subseasonal forecasts. Consistent with previous findings [1], negative PNA-like patterns are observed when MJO convection anomalies are in Phases 4 (Supplementary Figure 11). Notably, the FuXi-S2S model proficiently reproduces these anomalous circulation patterns, evidenced by its consistently high pearson correlation coefficient (PCC) even at extended forecast lead time (weeks 5 and 6). This model demonstrate superior PCC for MJO-associated Z500 patterns in FuXi-S2S compared to the ECMWF model across various lead times. As a result, the FuXi-S2S model's superior capability in MJO prediction and its accurate simulation of MJO teleconnections significantly enhance its performance in subseasonal forecasting, especially in extratropical regions.

Supplementary Figure 9 presents a comparative analysis of the bivariate correlation coefficient (COR) and error (ERROR) metrics for the amplitude and phase of the MJO. These metrics are derived from the ensemble mean of ECMWF S2S reforecasts and FuXi-S2S forecasts, averaged over all the testing data from 2017 to 2021. Among them, the COR reflects the accuracy of evolution, and ERROR indicates the systematic bias. The analysis reveals that COR values decline with increasing forecast lead times, with a more pronounced decrease observed for the MJO phase compared to the amplitude. Throughout the 42-day forecast period, the COR for MJO amplitude remains consistently above 0.8. The differences in amplitude COR between the ECMWF S2S and FuXi-S2S models are negligible. In contrast, FuXi-S2S consistently outperforms ECMWF S2S in phase COR, maintaining higher values over the entire forecast duration. Specifically, the COR for the MJO phase drops below 0.5 at 28 days for ECMWF S2S, whereas for FuXi-S2S, it remains above this threshold until 34 days. Additionally, negative error values for the MJO amplitude indicate that the amplitude is on average smaller in both the ECMWF S2S and FuXi-S2S simulations compared to ERA5 data, aligning with findings from previous studies [2, 3]. FuXi-S2S exhibits smaller errors than ECMWF S2S, suggesting it better maintains the amplitude of MJO events. Regarding the error in the MJO phase, both models show comparable values up to 32 days, indicating the small systematic phase speed error in both models. However, after 32 days, FuXi-S2S shows larger phase errors than ECMWF S2S. Overall, the superior performance of FuXi-S2S in predicting MJO compared to that of ECMWF S2S is primarily due to its enhanced ability to predict the MJO phase.

5 Extreme Meiyu in 2020

The major rainy season of the East Asian summer monsoon, called Meiyu in China [4], typically starts in early June and ends in mid-July. This brings abundant rainfall which accounts for the majority of the annual precipitation in China, Japan, and South Korea [5, 6]. In the summer of 2020, the Yangtze-Huaihe River valley (YHRV) experienced an exceptionally intense Meiyu rainy season characterized by an earlier onset and a delayed retreat. This season lasted for 62 days, making it one of the longest events since 1961, equalling the duration of the 2015 event [7]. The accumulated precipitation during the 2020 Meiyu season broke the historical record since 1961 and resulted in the most severe flooding in the YHRV in recent decades. By mid-July, the flooding had led to more than 140 fatalities or missing persons and economic losses of USD 11.75 billion.

Supplementary Figure 12 presents the comparison of the standardized TP anomaly among the observations sourced from Global Precipitation Climatology Project (GPCP), ECMWF S2S, and FuXi-S2S, averaged across YHRV bounded by 105 to 125°E in longitude and 25 to 35°N in latitude. The GPCP are temporally averaged over a two-week period from June 30th to July 13th, 2020, which corresponds to a low skill and cold-front rainy period as revealed by by Liu et al. [8]. FuXi-S2S forecasts and ECMWF S2S reforecasts were initialized on different dates. Notably, the ECMWF S2S model predicts negative TP anomalies for forecasts initialized on both June 2nd and June 6th. However, while the ECMWF S2S model starts to predict positive TP anomalies from June 9th onwards, the model consistently underestimates rainfall intensity. In contrast, the FuXi-S2S model predicts positive anomalies for forecasts initialized as early as June 2nd, offering a lead time of 4 weeks prior to the occurrence of the event. Furthermore, the spatial distributions of the standardized TP anomaly reveals that TP patterns predicted by FuXi-S2S closely aligns with the observations, which is critical for flood preparedness. In summary, FuXi-S2S demonstrates superior performance in predicting the intensity of extreme rainfall events with longer lead time compared to ECMWF S2S.

6 Comparisons against ECMWF S2S real-time forecasts

This study also evaluates the performance of FuXi-S2S by analyzing testing data from 2022 and compare against the 51-member ECMWF S2S real-time forecasts from model cycle C47r3. The evaluation included deterministic metrics of the ensemble mean, ensemble metrics, and MJO forecasts.

Supplementary Figure 13 presents a comparison of the globally-averaged and latitude-weighted TCC, RMSE, RPSS, and BSS of the ensemble mean between the ECMWF S2S real-time forecasts and FuXi-S2S forecasts for TP in 2022. Across all forecast lead times, FuXi-S2S demonstrates superior forecast performance in all metrics across compared to the ECMWF S2S real-time forecasts.

Supplementary Figure 14 presents the bivariate correlation (COR) skills of Real-time Multivariate MJO (RMM) index for the ensemble mean of ECMWF S2S real-time forecasts and FuXi-S2S forecasts, averaged over the testing data from 2022. When applying a COR threshold of 0.5 to determine skillful MJO forecast, FuXi-S2S extends the skilful forecast lead time from 30 days to 41 days, surpassing the performance of ECMWF S2S real-time forecasts.

7 Effectiveness of larger ensemble

Supplementary Figure 15 presents a comparison of the globally-averaged and latitude-weighted RPSS and BSS of the ensemble mean between the ECMWF S2S reforecasts, the 51-member FuXi-S2S forecasts, and the 101-member FuXi-S2S forecasts, for T2M and TP. This analysis encompasses all testing data spanning from 2017 to 2021. Notably, the 101-member FuXi-S2S demonstrate a significant improvement in forecast performance relative to the 51-member FuXi-S2S across all forecast lead times for both T2M and TP. This enhancement proves that an increase in the number of ensemble members improves the prediction skills in subseasonal forecasts.

8 Evaluation against the GPCP data

Supplementary Figure 16 and present a comparative analysis of the globally-averaged and latitude-weighted TCC and RPSS of the ensemble mean between ECMWF S2S reforecasts and FuXi-S2S forecasts for TP, based on testing data between 2017 and 2021. Unlike prior analyses, this evaluation employs the GPCP dataset as the reference, rather than the ERA5 dataset. Consistent with the results shown in Figure 1 of the main text and Supplementary Figure 6, where ERA5 serves as the verification target, the FuXi-S2S model generally outperforms ECMWF S2S at most forecast lead times, achieving higher TCC, RPSS, and BSS values than ECMWF S2S. However, an exception is noted in week 3, where ECMWF S2S exhibits superior RPSS values. Notably, since the FuXi-S2S is trained on TP data from the ERA5 dataset, its performance slightly diminishes when evaluated against the GPCP dataset. This reduction in performance is likely due to the discrepancies between the GPCP and ERA5 datasets. Considering the known differences between the ERA5 TP data and actual observations, as highlighted in [9, 10], exploration of more accurate TP data sources is planned to enhance the forecast accuracy of the FuXi-S2S model.

Supplementary Figures

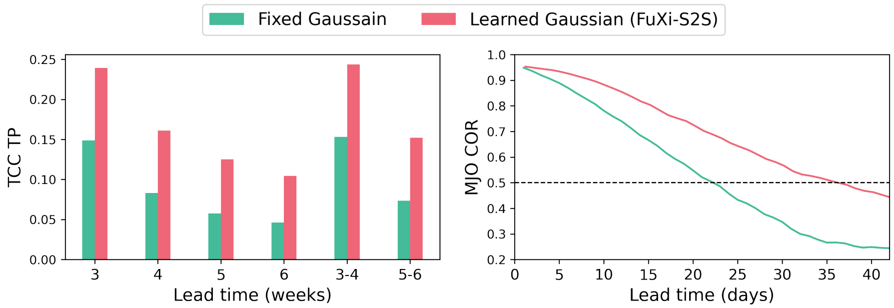

Supplementary Figure 1: Comparison of the FuXi-S2S model (in red) and FuXi-S2S with fixed Gaussian perturbations (in green), utilizing all testing data from 2017 to 2021. The first column is the comparison of the globally-averaged latitude-weighted TCC. The second column is the comparison of the globally-averaged latitude-weighted RMM bivariate COR of the FuXi-S2S (in red) and FuXi-S2S with fixed Gaussian noise (in light red) using testing data from 2017 to 2021. When the FuXi-S2S forecasts fail to show a statistically significant improvement over the ECMWF S2S reforecasts at the 97.5% confidence level, a pale color scheme is used to denote these results.

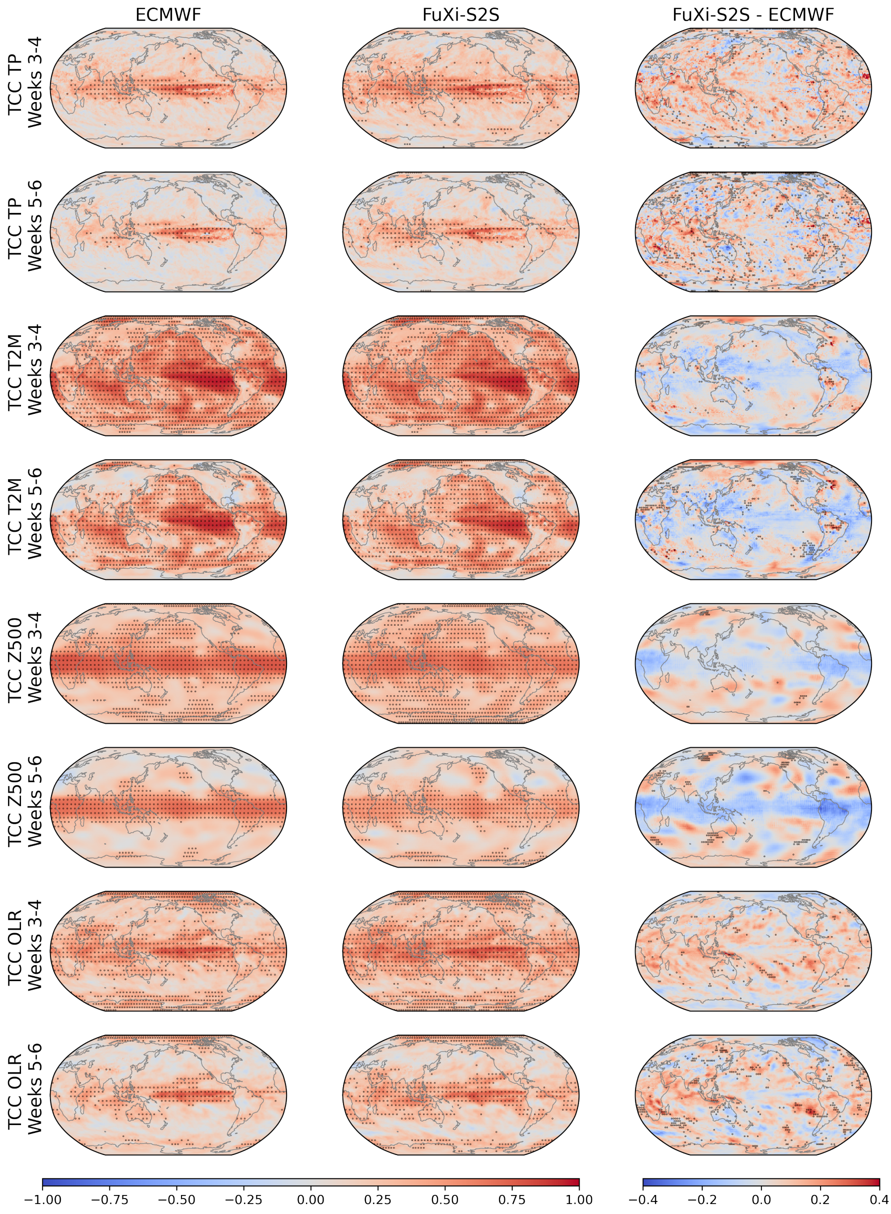

Supplementary Figure 2: Spatial map of average TCC without latitude weighting of ECMWF S2S (first column) and FuXi-S2S (second column), and the differences in TCC between FuXi-S2S and ECMWF S2S (third column) for TP (first and second rows), T2M (third and fourth rows), Z500 (fifth and sixth rows), and OLR (seventh and eighth rows) at forecast lead times of weeks 3-4 (first, third, fifth, and seventh rows), weeks 5-6 (second, fourth, sixth, and eighth rows), using all testing data between 2017 and 2021. Stippling on the map denotes areas where the skill score is statistically significant at the 97.5% confidence level. Specifically, in columns 1 and 2, stippling indicates regions where the skill scores of the ECMWF S2S and FuXi-S2S models significantly surpasses those of climatology. In column 3, stippling highlights areas where the FuXi-S2S model significantly outperforms the ECMWF S2S.

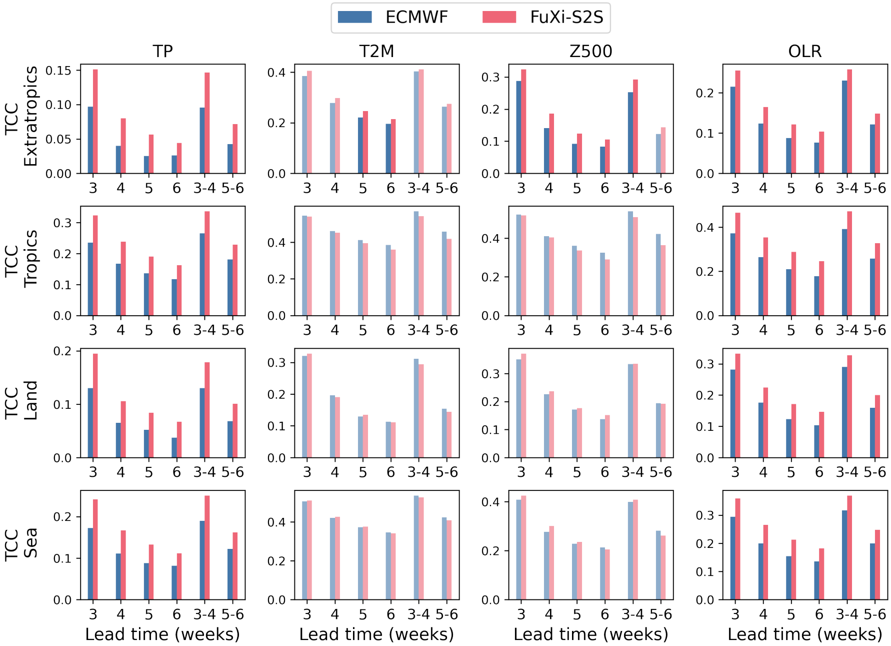

Supplementary Figure 3: Comparison of the latitude-weighted TCC of the ensemble mean of ECMWF S2S (in blue) forecasts and FuXi-S2S forecasts (in red) for TP (first column), T2M (second column), Z500 (third column), and OLR (fourth column) averaged over extra-tropics (90°S - 30°S and 30°N - 90°N, first row), tropics (30°S - 30°N, second row), land (third row), and sea (fourth row), using all testing data between 2017 and 2021. When the FuXi-S2S forecasts fail to show a statistically significant improvement over the ECMWF S2S reforecasts at the 97.5% confidence level, a pale color scheme is used to denote these results.

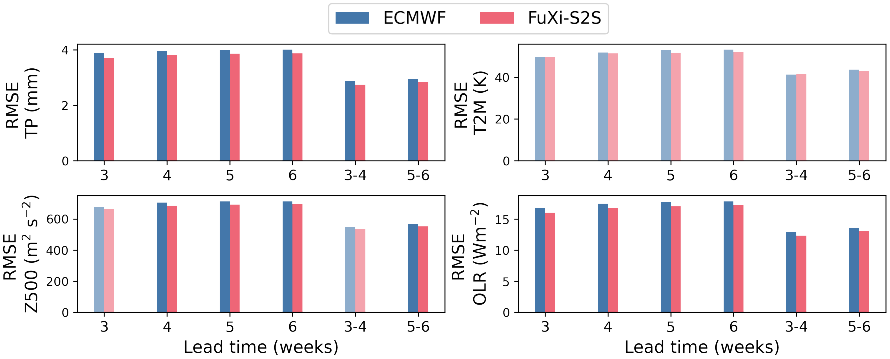

Supplementary Figure 4: Comparison of the globally-averaged and latitude-weighted RMSE of the ensemble mean between ECMWF S2S reforecasts (in blue) and FuXi-S2S forecasts (in red) for TP, T2M, Z500, and OLR, using all testing data between 2017 and 2021. A bootstrapping approach, repeated 1000 times, is used for significance testing. When the FuXi-S2S forecasts fail to show a statistically significant improvement over the ECMWF S2S reforecasts at the 97.5% confidence level, a pale color scheme is used to denote these results. It is important to note that TP here refers to 24-hour accumulated precipitation.

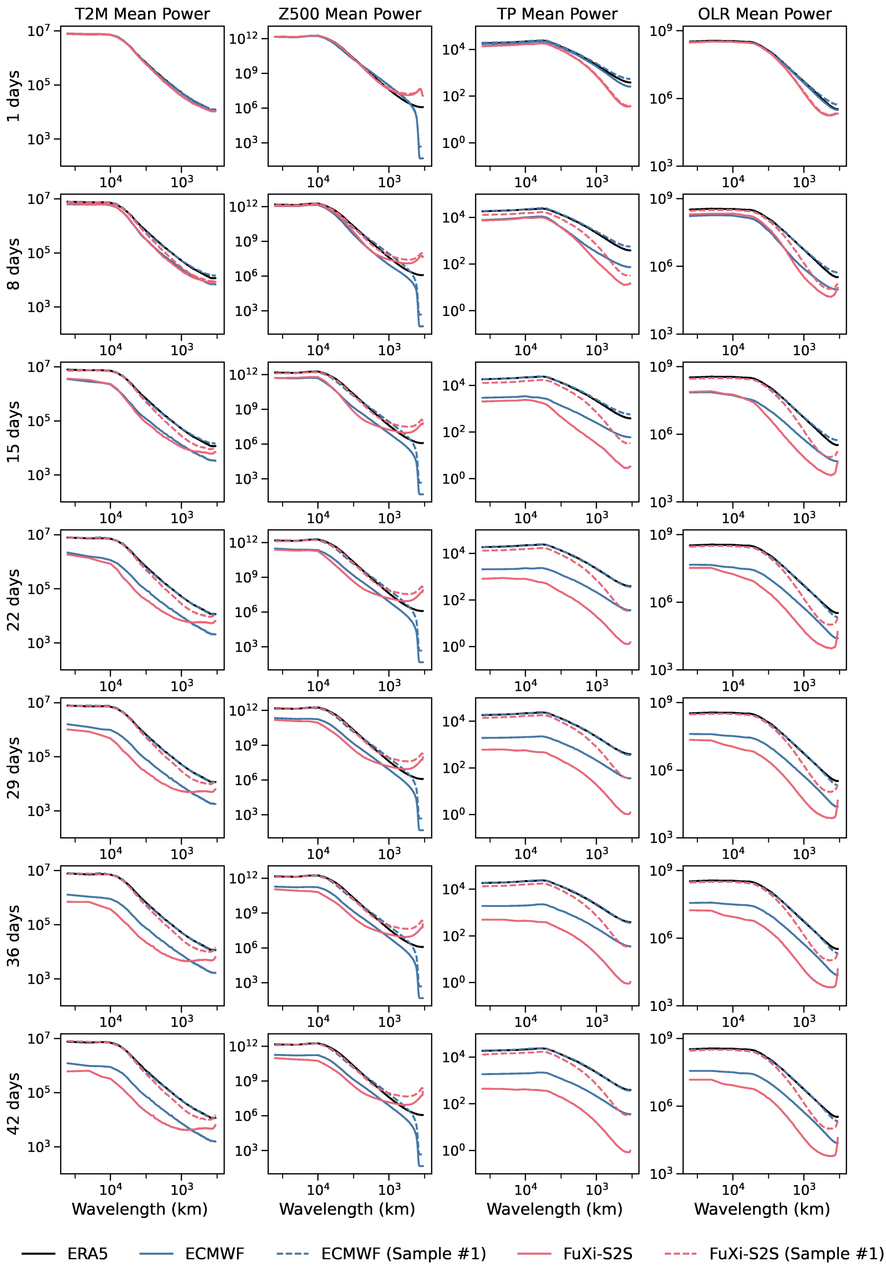

Supplementary Figure 5: Energy spectra of T2M (first row) and TP (second row) for ERA5 (in black), ECMWF S2S (in blue) reforecasts and FuXi-S2S forecasts (in red) at forecast lead times of 15 days (first column), 22 days (second column), 29 days (third column), 36 days (fourth column), and 42 days (fifth column), using all testing data between 2017 and 2021.

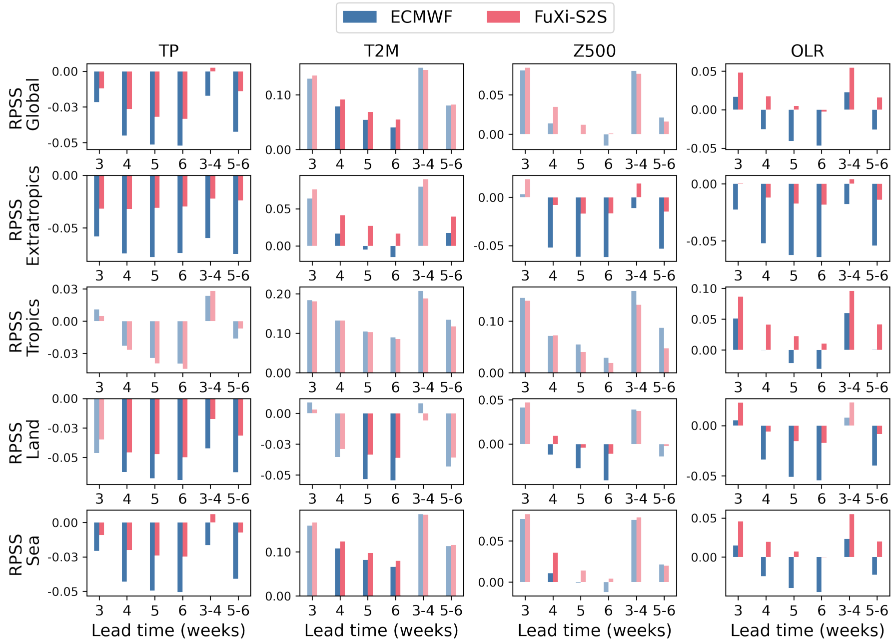

Supplementary Figure 6: Comparison of the latitude-weighted RPSS of ECMWF S2S (in blue) forecasts and FuXi-S2S forecasts (in red) for TP (first column), T2M (second column), Z500 (third column), and OLR (fourth column) averaged over extra-tropics (90°S - 30°S and 30°N - 90°N, first row), tropics (30°S - 30°N, second row), land (third row), and sea (fourth row), using all testing data between 2017 and 2021. When the FuXi-S2S forecasts fail to show a statistically significant improvement over the ECMWF S2S reforecasts at the 97.5% confidence level, a pale color scheme is used to denote these results.

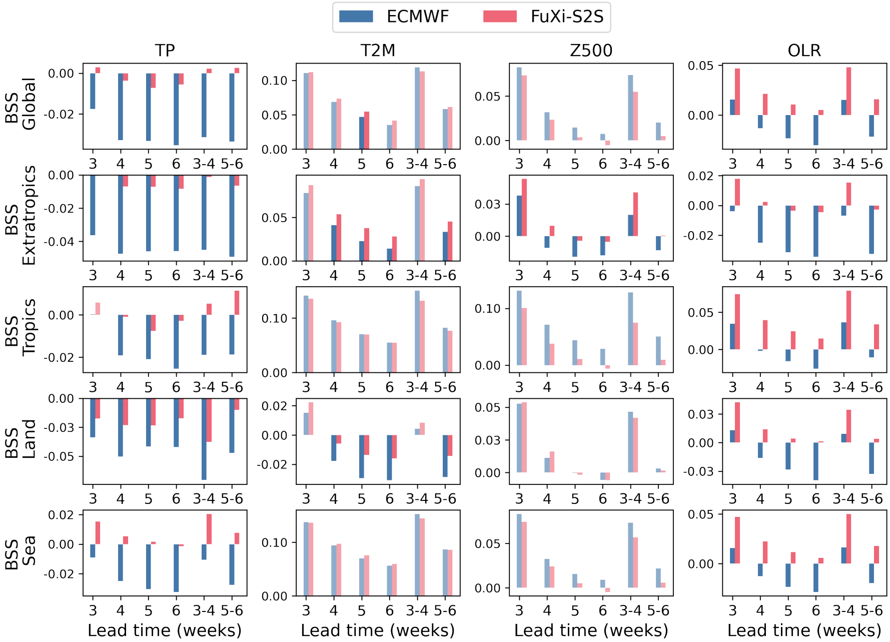

Supplementary Figure 7: Comparison of the latitude-weighted BSS of the ensemble mean of ECMWF S2S (in blue) forecasts and FuXi-S2S forecasts (in red) for TP (first column), T2M (second column), Z500 (third column), and OLR (fourth column) averaged over extra-tropics (90°S - 30°S and 30°N - 90°N, first row), tropics (30°S - 30°N, second row), land (third row), and sea (fourth row), using all testing data between 2017 and 2021. When the FuXi-S2S forecasts fail to show a statistically significant improvement over the ECMWF S2S reforecasts at the 97.5% confidence level, a pale color scheme is used to denote these results.

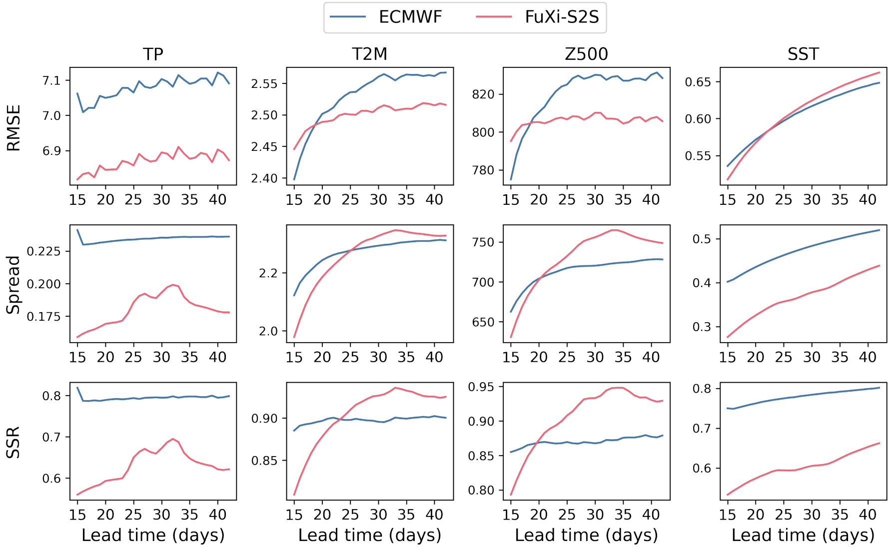

Supplementary Figure 8: Comparison of the globally-averaged, latitude-weighted RMSE, ensemble spread, and SSR of ECMWF S2S reforecasts (in blue), and FuXi-S2S forecasts (in red) for TP, T2M, and SST as a function of forecast lead times. This analysis includes all testing data between 2017 and 2021, using the daily mean forecasts to calculate these metrics. When the FuXi-S2S forecasts fail to show a statistically significant improvement over the ECMWF S2S reforecasts at the 97.5% confidence level, a pale color scheme is used to denote these results.

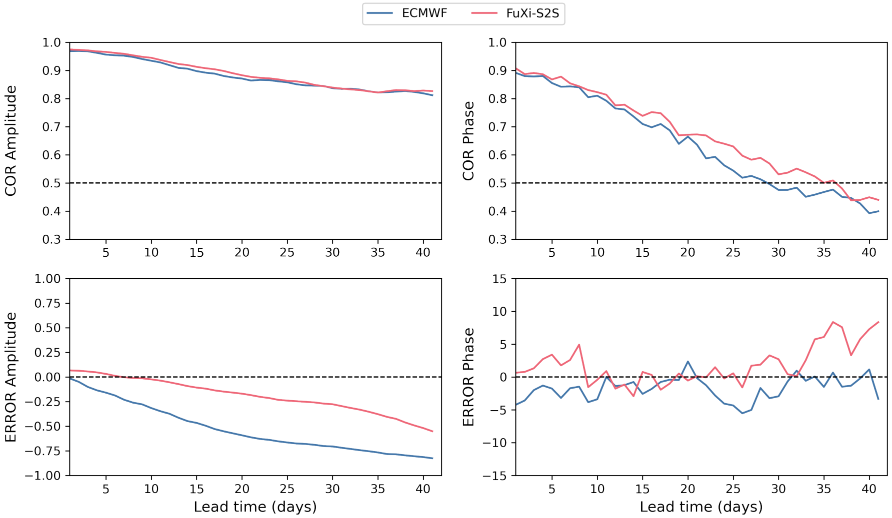

Supplementary Figure 9: Comparison of correlation (COR) (first row) and error (ERROR) (second row) in the amplitude (first column) and phase (second column) of the MJO of the ensemble mean between ECMWF S2S reforecasts (in blue) and FuXi-S2S forecasts (in red) using all testing data from 2017 to 2021. Dashed black line signifies the prediction skill threshold of COR=0.5 and ERROR=0.

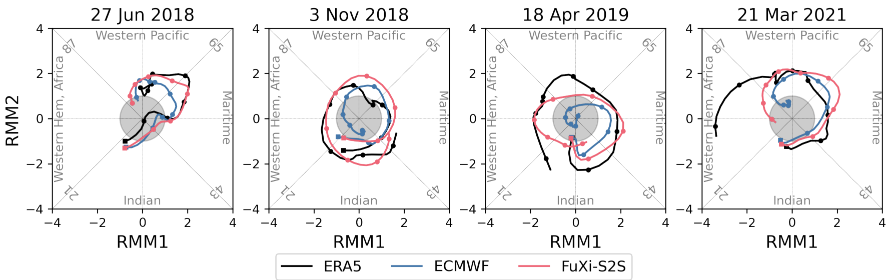

Supplementary Figure 10: Comparison of the RMM composite phase–space diagram for the observed MJO derived from the combination of CBO and ERA5 reanalysis data (in black) and the ensemble mean of ECMWF S2S reforecasts (in blue), and FuXi-S2S forecasts (in red). RMM1 and RMM2 are the x axis and y axis, respectively. The numbers within each octant (from 1 to 8) are the defined MJO phase, and the words on each side of the diagram describe the approximate location of MJO associated convection along the equator. Squares represent forecasts on day 1 and closed circles represent every 5 days from the forecast initialization time (open squares). The panels are for different initialization date: 27 June 2018, 3 November 2018, 18 April 2019, and 21 March 2021.

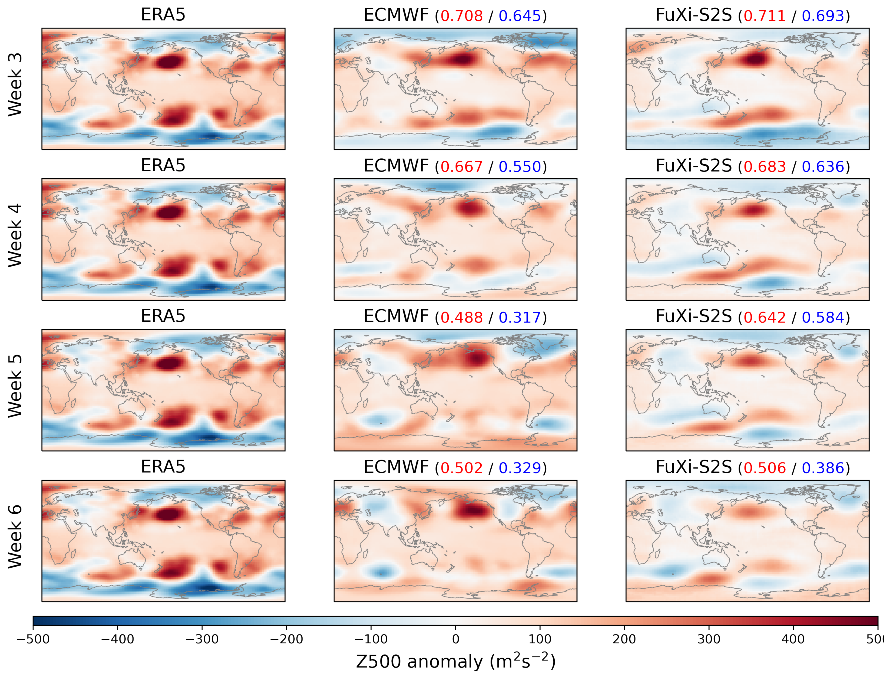

Supplementary Figure 11: Composite map of Z500 anomalies derived from ERA5 reanalysis data (first column), ECMWF S2S reforecasts (second column) and FuXi-S2S forecasts (third column). These maps cover forecast lead times of weeks 3, 4, 5, and 6, represented in the first, second, third, and fourth rows, respectively. All maps use testing data between 2017 and 2021, corresponding to initial forecast periods when the MJO is in phase 4 of its lifecycle. Red and blue numbers in columns 2 and 3 represent latitude-weighted pearson correlation coefficient (PCC) averaged globally and over extra-tropics (90°S - 30°S and 30°N - 90°N), respectively.

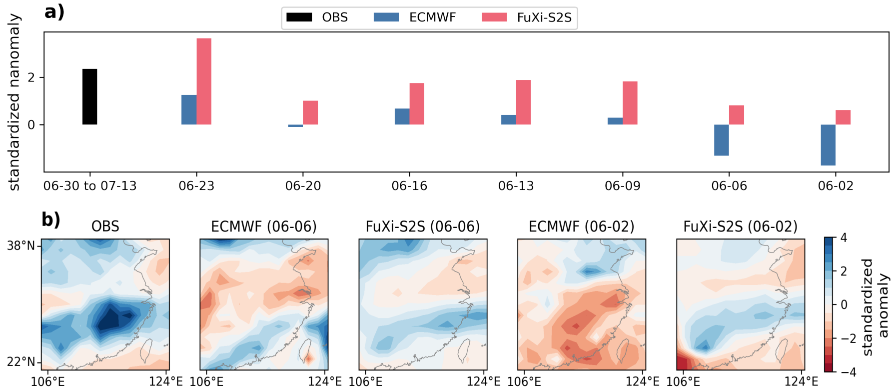

Supplementary Figure 12: Comparison of the spatially and temporally averaged standardised TP anomaly (a) for the 2 weeks from June 30th to July 13th, 2020 for GPCP observation (in black) and the predictions from ECMWF S2S reforecasts (in blue) and FuXi-S2S forecasts (in red), with initialization dates: June 23rd (06-23, MM-DD), June 20th (06-20), June 16th (06-16), June 13th (06-13), June 9th (06-09), June 6th (06-06), and June 2nd (06-02). Comparison of the temporally averaged standardised TP anomaly maps (b) for GPCP observation (first column) and predictions from ECMWF S2S (second column) and FuXi-S2S (third column), with initialization dates on June 6th (06-06, first row), and June 2nd (06-02, second row).

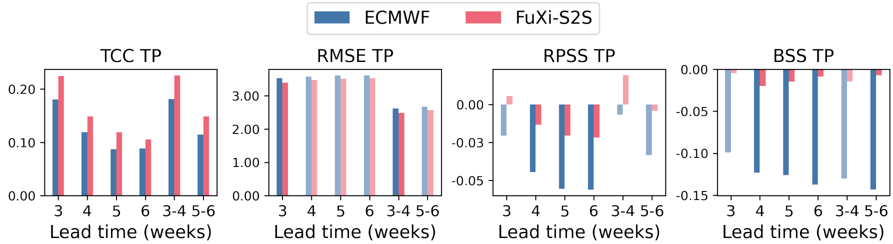

Supplementary Figure 13: Comparison of the globally-averaged latitude-weighted TCC (first column), RMSE (second column), RPSS (third column), and BSS (fourth column) between ECMWF S2S real-time forecasts (in blue) and FuXi-S2S forecasts (in red) for TP, using testing data from 2022. When the FuXi-S2S forecasts do not demonstrate a statistically significant improvement over the ECMWF S2S reforecasts, a pale color scheme is used to denote these results. It is important to note that TP here refers to 24-hour accumulated precipitation. When the FuXi-S2S forecasts fail to show a statistically significant improvement over the ECMWF S2S reforecasts at the 97.5% confidence level, a pale color scheme is used to denote these results.

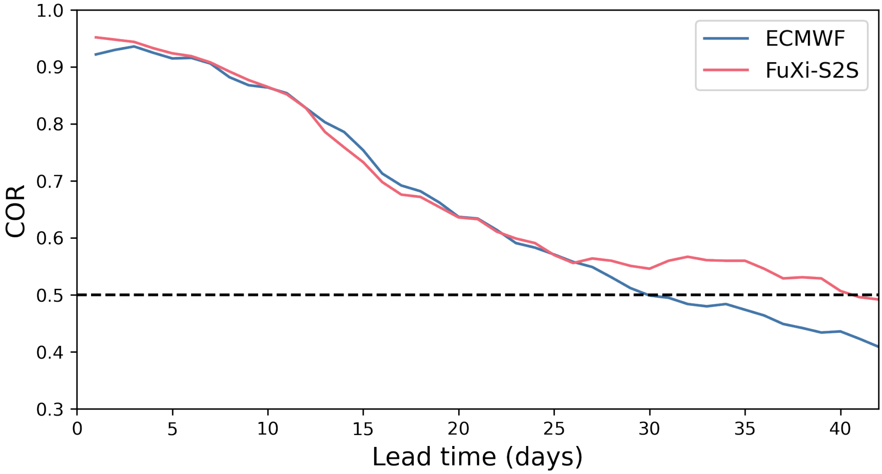

Supplementary Figure 14: Comparison of the globally-averaged latitude-weighted RMM bivariate COR (left column) of the ensemble mean of ECMWF S2S real-time forecasts (in blue) and FuXi-S2S forecasts (in red) using testing data from 2022, with dashed black lines indicating the prediction skill threshold of COR=0.5.

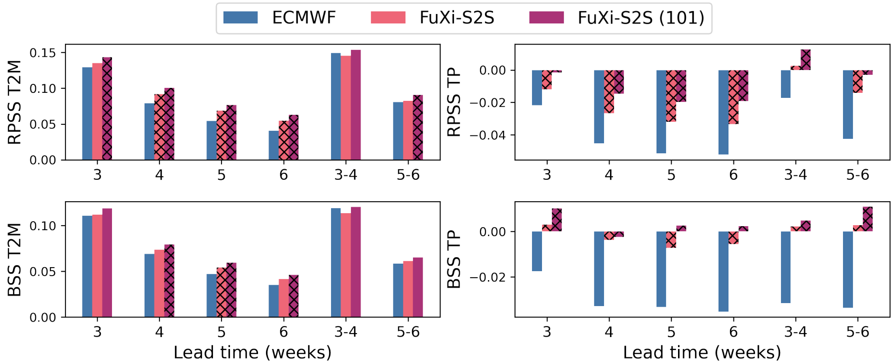

Supplementary Figure 15: Comparison of the globally-averaged latitude-weighted RPSS (first row) and BSS (second row) between ECMWF S2S reforecasts (in blue), 51-member FuXi-S2S forecasts (in red), and 101-member FuXi-S2S forecasts (in purple) for T2M and TP, using testing data from 2017 to 2021. When the 51-member FuXi-S2S forecasts or 101-member FuXi-S2S forecasts demonstrate a statistically significant improvement over the ECMWF S2S reforecasts at the 97.5% confidence level, a cross-line on the bar plot is used to denote these results.

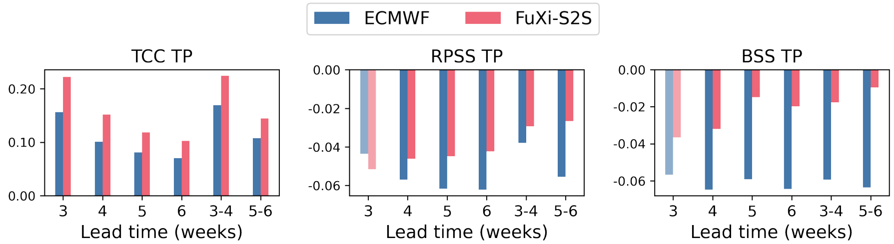

Supplementary Figure 16: Comparison of the globally-averaged and latitude-weighted TCC, RPSS, and BSS between ECMWF S2S reforecasts (in blue) and FuXi-S2S forecasts (in red) for TP, using all testing data between 2017 and 2021. Notably, verification is conducted with the GPCP dataset, rather than ERA5 dataset. When the FuXi-S2S forecasts fail to show a statistically significant improvement over the ECMWF S2S reforecasts at the 97.5% confidence level, a pale color scheme is used to denote these results.

Supplementary Tables

Supplementary Table 1: Optimizer hyperparameters

Optimizer	AdamW
LR decay schedule	Cosine
Number of GPUs used	8
Batch size	1 per GPU
Peak LR	2.5e-4
Weight decay	0.1
Total training steps	17,000

Supplementary References

[1] Seo, K.-H., Lee, H.-J.: Mechanisms for a pna-like teleconnection pattern in response to the mjo. Journal of the Atmospheric Sciences **74**(6), 1767–1781 (2017)

[2] Vitart, F., Woolnough, S., Balmaseda, M.A., Tompkins, A.M.: Monthly forecast of the madden–julian oscillation using a coupled gcm. Monthly Weather Review **135**(7), 2700–2715 (2007). https://doi.org/10.1175/MWR3415.1

[3] Vitart, F., Molteni, F.: Simulation of the madden–julian oscillation and its teleconnections in the ecmwf forecast system. Quarterly Journal of the Royal Meteorological Society **136**(649), 842–855 (2010). https://doi.org/10.1002/qj.623

[4] TAO, S.-Y.: A review of recent research on the east asian summer monsoon in china. Monsoon meteorology, 60–92 (1987)

[5] Ding, Y.: Summer monsoon rainfalls in china. Journal of the Meteorological Society of Japan. Ser. II **70**(1B), 373–396 (1992)

[6] Yihui, D., Chan, J.C.: The east asian summer monsoon: an overview. Meteorology and Atmospheric Physics **89**(1-4), 117–142 (2005)

[7] Liu, Y., Ding, Y.: Characteristics and possible causes for the extreme meiyu in 2020. Meteorological Monthly **46**(11), 1393–1404 (2020)

[8] Liu, B., Yan, Y., Zhu, C., Ma, S., Li, J.: Record-breaking meiyu rainfall around the yangtze river in 2020 regulated by the subseasonal phase transition of the north atlantic oscillation. Geophysical Research Letters **47**(22), 2020–090342 (2020)

[9] Nogueira, M.: Inter-comparison of era-5, era-interim and gpcp rainfall over the last 40 years: Process-based analysis of systematic and random differences. Journal of Hydrology **583**, 1–17 (2020)

[10] Lavers, D.A., Simmons, A., Vamborg, F., Rodwell, M.J.: An evaluation of era5 precipitation for climate monitoring. Q. J. R. Meteorol. Soc. **148**(748), 3152–3165 (2022). https://doi.org/10.1002/qj.4351